Measurements and analysis of turbulent consumption speeds of H_2/CO mixtures

Prabhakar Venkateswaran [a,*], Andrew Marshall [b], Dong Hyuk Shin [a], David Noble [a], Jerry Seitzman [a], Tim Lieuwen [a]

[a] School of Aerospace Engineering, Georgia Institute of Technology, Atlanta, GA 30332-0150, USA
[b] School of Mechanical Engineering, Georgia Institute of Technology, Atlanta, GA 30332-0405, USA

ARTICLE INFO

ABSTRACT

This paper describes measurements of global turbulent consumption speeds, $S_{T,GC}$, of hydrogen/carbon monoxide (H_2/CO) mixtures. The turbulent flame properties of such mixtures are of fundamental interest because of their strong stretch sensitivity, and of practical interest since they are the primary constituents of syngas fuels. Data are reported at mean flow velocities and turbulence intensities of $4 < U_0 < 50$ m/s and $1 < u'_{rms}/S_{L,0} < 100$, respectively, for H_2/CO blends ranging from 30% to 90% H_2 by volume. Two sets of experiments are reported. In the first, fuel blends ranging from 30% to 90% H_2 and mixture equivalence ratio, ϕ, were adjusted at each fuel composition to have nominally the same unstretched laminar flame speed, $S_{L,0}$. In the second set, equivalence ratios were varied at constant H_2 levels. The data clearly corroborate results from other studies that show significant sensitivity of $S_{T,GC}$ to fuel composition. In particular, at a fixed u'_{rms} and $S_{L,0}$, values of $S_{T,GC}$ increase by a factor of almost 2 when H_2 levels are increased from 30% (at $\phi = 0.61$) to 90% (at $\phi = 0.48$). Moreover, $S_{T,GC}$ in the 90% H_2 case is three times larger than the $\phi = 0.9$ CH_4/air mixture with the same $S_{L,0}$ value. An important conclusion from this work is these fuel effects are not simply a low turbulence intensity phenomenon – they clearly persist over the entire range of turbulence intensities used in the measurements. We also describe physics-based correlations of these data, using leading points concepts and detailed kinetic calculations of the stretch sensitivity of these mixtures. These results are used to develop an inequality for negative Markstein length flames that bounds the turbulent flame speed data and show that the data can be collapsed using the maximum stretched laminar flame speed, $S_{L,max}$, rather than $S_{L,0}$.

© 2011 The Combustion Institute. Published by Elsevier Inc. All rights reserved.

1. Introduction

This paper describes measurements of global consumption speeds, $S_{T,GC}$, of hydrogen/carbon monoxide (H_2/CO) fuel mixtures. The turbulent flame properties of such mixtures are of fundamental interest because of their strong stretch sensitivity. Stretch effects on turbulent flame speeds remain an issue in the turbulent combustion literature that requires clarification. H_2/CO mixtures are also of practical interest in the study of syngas fuels, which are primarily composed of H_2 and CO [1]. The turbulent flame speed of such mixtures has important influences on many important combustor operational issues, such as thermal loading, blow-off limits, flashback limits, and combustion instability [2].

Numerous studies have discussed turbulent flame speed correlations of the form $S_T = S_{L,0} \cdot f(u'_{rms})$, where u'_{rms} denotes the root-mean-square (RMS) turbulence fluctuations [3,4]. However, as shown repeatedly in the literature, u'_{rms} and $S_{L,0}$ alone do not capture many important characteristics of the turbulent flame speed [3]. It is also significantly affected by mean flow velocity [5], length scale [6–8], and fuel composition – it is this latter sensitivity which is a key focus of this study. For example, Kido et al. [9,10] obtained data for mixtures of H_2, methane (CH_4), and propane (C_3H_8) where, by adjusting the dilution and stoichiometries of the different fuel blends, they obtained different mixtures with the same unstretched laminar flame speed, $S_{L,0}$. Their data clearly show that these mixtures have substantially different turbulent flame speeds, with the high H_2 mixtures having an order of magnitude larger S_T value than the propane mixture. Thus, two different fuel mixtures can have appreciably different turbulent flame speeds, despite having the same un-stretched laminar flame speed, turbulence intensity and burner configuration.

Many studies showing these fuel effects have been compiled in the review paper of Lipatnikov and Chomiak [3], and an updated discussion of stretch effects is provided by Driscoll [11]. These fuel effects are believed to be associated with stretch sensitivity of the reactive mixture, that is, in turn, a function of differences in the relative rates of mass and/or thermal diffusion of the deficient species

[12]. Stretch sensitivity leads to variations in the local burning rate along the turbulent flame front. For example, the burning rate of the positively strained leading points of the turbulent flame is increased for mixtures with negative Markstein lengths, l_M [12]. Studies by Kido et al. [10] have shown that fuel/air mixtures with negative Markstein lengths (e.g., lean methane or hydrogen flames) have higher turbulent flame speeds than those that are relatively stretch insensitive, which, in turn, exceed those with positive Markstein lengths (e.g., lean propane–air flames). For syngas fuels, this effect is particularly important because of the large differences in diffusivity of the various fuel constituents (e.g., H_2 and CO, plus the diluents carbon dioxide (CO_2), nitrogen (N_2), and water (H_2O)) with respect to each other and to air.

The measurements reported in this paper had two primary motivations. First, limited data are available for H_2/CO fuel mixtures; a few examples are from Daniele et al. [13,14] and Karpov and Severin [15]. Second, much of the turbulent flame speed data where strong stretch effects may be present have been obtained at turbulence intensities, $u'_{rms}/S_{L,0}$, often less than 20 [9,10,16–21]. Obtaining such data at high turbulence intensities is of fundamental interest to explore the relative roles and interactions between turbulent stretching of the flame front and its stretch sensitivity, in particular whether stretch effects change with turbulence intensity. The above studies suggest that fuel effects persist at higher turbulence intensities, but further data are needed to validate this point. A key contribution of this study is obtaining data over a range of H_2/CO mixtures at turbulence intensities, $u'_{rms}/S_{L,0}$, up to 100. We conclude that fuel effects on the turbulent flame speed are an important issue across the entire range of turbulence intensities used in these measurements.

In addition to the measurements, we report efforts to correlate these data using a physics-based model incorporating the leading points concept [3,8,22], which provides a helpful approach for incorporating modern understanding of stretch sensitivities of these flames [12] into data analysis.

2. Experimental approach and facility

This section describes the approach and experimental facility used to quantify the turbulent flame speed. As noted above, $S_{T,GC}$ is a property of not only the fuel–air mixture, but also the flow. As such, well characterized, highly reproducible burners whose results can be compared to other workers and data are critical to these measurements [23].

We start with some discussion of the measurement approach. This is an important issue because of the definition dependence of S_T. Extensive discussion of the merits and drawbacks of various approaches are contained in the literature. Some resolution has been achieved in two recent reviews [11,24] and through the International Workshop on Premixed Flames [25], where it is noted that there are actually multiple useful definitions for S_T that are relevant for different combustion issues (e.g., flashback versus heat release per volume). Four definitions of S_T have been proposed: local displacement speed, $S_{T,LD}$, global displacement speed, $S_{T,GD}$, local consumption speed, $S_{T,LC}$, and global consumption speed, $S_{T,GC}$ [11,24,25].

The local consumption and displacement speeds attempt to quantify the local propagation rate and mass burning rate of the turbulent front, respectively. There are various challenges associated with defining these quantities locally, however. For example, the definition of $S_{T,LC}$ is:

$$S_{T,LC} = S_{L,0} I_0 \int_{-\infty}^{\infty} \Sigma d\eta \tag{1}$$

where $S_{L,0}$, I_0 and Σ are the un-stretched laminar flame speed, stretch factor and the flamelet surface area per unit volume

respectively. Clearly, this integral is a function of the integration path, η, through the turbulent flame brush. Several authors suggest that it be performed in a direction normal to the flame brush [11], which is itself generally a function of reaction progress variable.

Difficulties associated with defining a local value of S_T can be circumvented to some extent by defining global burning rates (assuming, of course, that all the reactant mass flow pass through the flame brush [11]), at the cost of averaging over potentially substantial variations in local burning rates for cases where the flame brush is spatially evolving. However, global turbulent flame speeds are also definition dependent. For example, $S_{T,GC}$ is defined as:

$$S_{T,GC} = \frac{\dot{m}_R}{\rho_R \overline{A}_{\langle c \rangle}} \tag{2}$$

where $\dot{m}_R$, ρ_R and $\overline{A}_{\langle c \rangle}$ denote reactant mass flow rate, reactant density and mean flame area corresponding to some prescribed $\langle c \rangle$ contour. Thus, the value of $S_{T,GC}$ is itself a function of the progress variable surface used to define the mean flame front area.

This study focuses upon measurements of $S_{T,GC}$ using a turbulent Bunsen flame, an $S_{T,GC}$ measurement approach recommended by Gouldin and Cheng [25]. This configuration was used because of the wide variety of available data in similar geometries for benchmarking and comparisons, such as the extensive data sets from Kobayashi's group [21,23,26,27].

A schematic of the system is shown in Fig. 1. The burner is a smoothly contoured nozzle with high contraction ratio to inhibit boundary layer growth and to achieve a top hat exit velocity profile. Measurements were taken using burners with 12 and 20 mm exit diameters. An annular sintered plate is placed around the burner outlet to hold a premixed, methane–air pilot flame, needed to stabilize the main flame at the higher flow velocities used in this study. The total mass flow rate of the pilot does not exceed 5% of the main flow rate to ensure minimal impact of the pilot on the main flame. This was checked by taking measurements with various pilot flow rates.

Mass flow rates of the fuel and air for both the main and pilot flames are metered using mass flow controllers that have accuracies of ±1.5% of the full scale. As a result, equivalence ratios quoted here have uncertainties ranging from 3% to 5%, depending on the full-range scale of the mass flow controllers used.

The fuel/air mixture is premixed 2 m ahead of the burner. Upon entering the main burner assembly, the flow passes through a layer of ball bearings to minimize "jetting" effects from the smaller diameter reactant feed lines.

The turbulence intensity is varied independently of the mean flow velocity using a remotely controlled turbulence generator. This turbulence generator assembly consists of milled slots in a thin plate that cause flow separation and vorticity generation as the flow passes through them. These vortical structures impinge on the inclined wall of the converging section of the nozzle, breaking them down into finer turbulent eddies [28–30].

As shown in Fig. 1, the turbulence generating plates are secured 84 mm upstream of the burner exit. Prior implementations of these turbulence generators used fixed plates [28–30] – different blockage ratio plates were manufactured to vary turbulence intensity. In this study, substantial effort was devoted to developing a system that is continuously variable, in order to sweep out a range of turbulence intensities at a fixed mean flow velocity. This capability is also needed to facilitate the high-pressure measurements that are planned for the next phase of experiments. This system consists of a 3 mm thick bottom plate that is secured to the plenum and a 6 mm thick top plate attached to a central shaft that is connected to a stepper motor. This configuration allows for variable degrees of blockage as shown in Fig. 2.
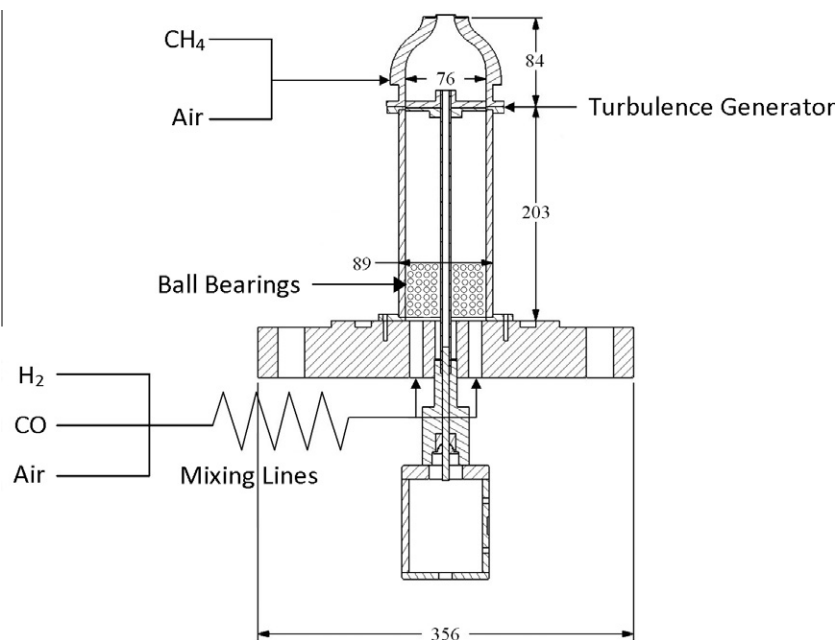
Fig. 1. Schematic of the experimental facility. Dimensions in mm.

The plate's angular position is measured with an optical enco-der to an accuracy of ±0.1°. The stepper motor is connected to the central shaft via a worm gear, minimizing backlash. Maximum and minimum blockage possible with this setup is 97% and 69%, corresponding to an angular opening of 1.5° and 30°, respectively. Turbulence intensity increases monotonically with increasing blockage ratio.

At very high blockage ratios, the mixture passes through the slots at an angle, leading to some swirl in the flow. This effect was reduced somewhat by the addition of straighteners as shown in Fig. 3, but it still imposes a maximum blockage ratio over which data are obtained. We utilized the criterion that the maximum blockage ratio remains less than 93% for all flame speed data pre-sented in this paper, based upon the flow field characterization de-scribed in the next section.

2.1. Flow field characterization

The flow field was characterized using 3-component Laser Doppler Velocimetry (LDV). The air flow was seeded using 5 μm alumina (Al_2O_3) particles and the flow field velocity at the burner exit was mapped using a TSI 3-component LDV system mounted on a computer-controlled, three-axis traverse to enable axial and radial scanning across the burner exit along three orthogonal directions. The LDV system comprised of a 5 W argon ion laser with an FBL-3 multicolor beam generator. Two fiber optic transceiver probes were mounted 90° apart and operated in backward-scatter mode. The signal from the transceiver probe was connected to a PDM 1000-3 three-channel photodetector module and the output was processed by an FSA 3500-3 signal processor to record three components of velocity in non-coincidence mode. The typical number of realizations used to generate the quoted velocity statis-tics we about 10,000 counts on the axial channel and over 1000 on the radial and azimuthal channels.

Data were obtained at mean flow velocities from U_0 = 4–50 m/s, which correspond to $Re_D = U_0D/\nu$ = 5100–64,000. The turbulence intensities quoted below, u'_{rms}, are based upon the total turbulence intensity using all three velocity components; i.e., $u'_{rms} = \sqrt{\overline{u'^2} + \overline{v'^2} + \overline{w'^2}}$. As such, some care should be taken when compar-ing with other data in the literature, such as when measurements are obtained with hot wire anemometers that capture two velocity components.

Figures 4–6 plot representative profiles of the mean and fluctu-ating axial, radial and azimuthal velocities as a function of the ra-dial location of the 20 mm diameter burner at 50 m/s at three different blockage ratios.

The data show a well-defined top-hat mean axial velocity, along with low radial velocity. The mean azimuthal velocity increases with increasing blockage ratio, as discussed earlier. It should be noted that the time-averaged mean and fluctuating velocity pro-files are flat, except in the boundary layer, and that as the blockage
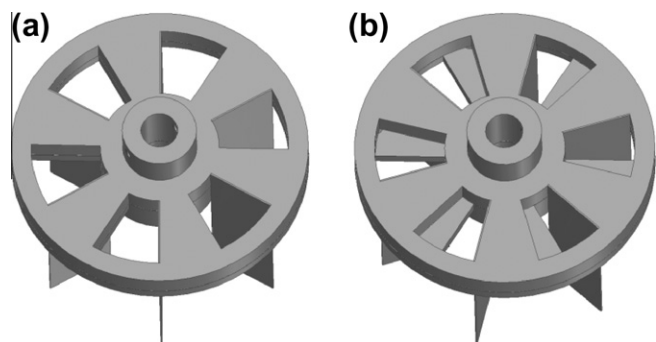

Fig. 2. Schematic of the turbulence generating plates: (a) fully open and (b) partially closed.
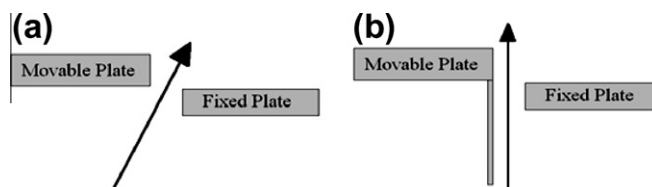

Fig. 3. Flow characteristics (a) without and (b) with flow straighteners.
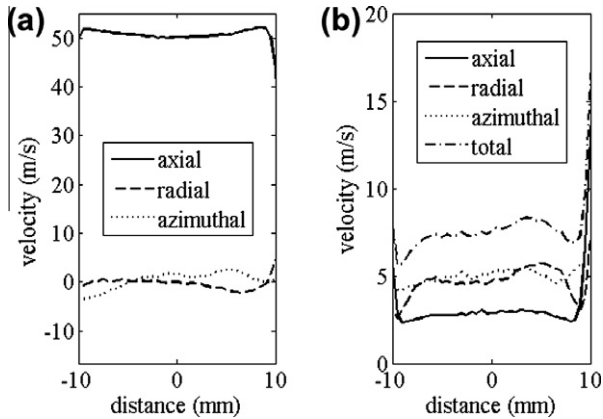
Fig. 4. Plots of (a) mean axial, radial and azimuthal velocities and (b) fluctuating axial, radial, and azimuthal and total fluctuating velocities as a function of radial distance from center of the burner for $U_0 = 50$ m/s at a blockage ratio of 69%.
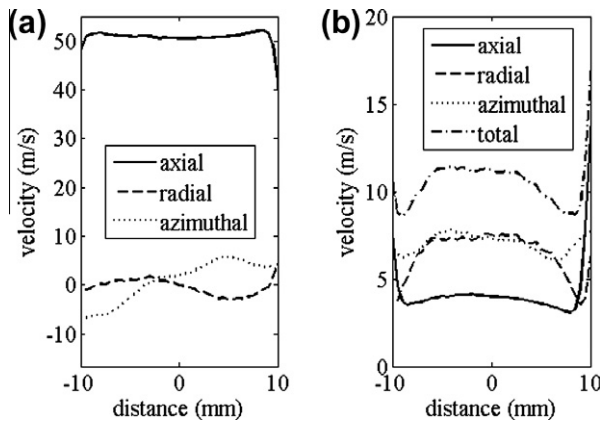

Fig. 5. Plots of (a) mean axial, radial and azimuthal velocities and (b) fluctuating axial, radial, and azimuthal and total fluctuating velocities as a function of radial distance from center of the burner for $U_0 = 50$ m/s at a blockage ratio of 81%.
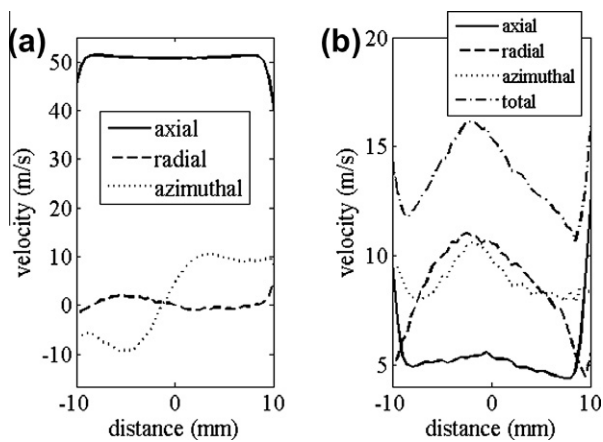

Fig. 6. Plots of (a) mean axial, radial and azimuthal velocities and (b) fluctuating axial, radial, and azimuthal and total fluctuating velocities as a function of radial distance from center of the burner for $U_0 = 50$ m/s at a blockage ratio of 93%.

ratio is increased from 69% in Fig. 4 to 93% in Fig. 6, the turbulence intensity monotonically increases.

Figure 7 summarizes the performance of the turbulence generator, by plotting the dependence of the centerline turbulence intensity, u'_{rms}/U_0, upon blockage ratio. It shows that the turbu-
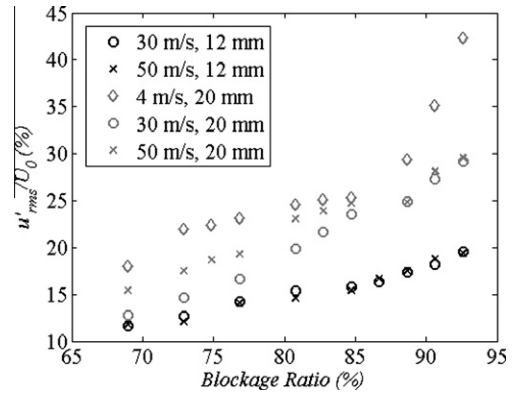

Fig. 7. Dependence of burner centerline total turbulence intensity (i.e. summed over all three fluctuating velocity components) upon blockage ratio.

lence intensity monotonically increases with blockage ratio. Turbulence intensities obtained with the 12 mm burner are lower than that obtained with the 20 mm burner at the same blockage ratio. This occurs because, at a fixed nozzle exit velocity, the flow velocity through the blockage plate gaps is lower for the smaller burner.

An important question for configurations such as used here, where the turbulence intensity varies radially and axially, and where there is strong shear generated turbulence, is the appropriate turbulence intensity that should be used to characterize u'_{rms}. While we do not weigh in on this question here, we do note that the centerline turbulence intensity scales well with that at other locations. To illustrate, Fig. 8 presents a comparison between the shear (or, more precisely, u'_{rms} at $r = 10$ mm) and centerline turbulence intensities. Note the one-to-one correspondence between the two, with $u'_{rms}(r = 10\text{ mm}) = 0.87u'_{rms}(r = 0\text{ mm}) + 6.9U_0$.

Limited particle image velocimetry (PIV) were also conducted to map the entire flow field and determine the axial dependence of the turbulence intensity. Figure 9 shows the mean and RMS velocity fields normalized by the mean centerline velocity at the burner exit. Note that the centerline turbulence intensity remains relatively constant, and actually grows slightly for at least the first 50 mm downstream, typical of jet turbulence [31]. This is important since it implies that the turbulence intensity at the flame front is approximately the same as the intensity at the burner exit.

Figure 10 presents typical 1-D turbulent power spectra at the burner centerline for several blockage ratios, scaled by u_{rms}^2. The data were obtained from hot wire time series data, described later. The spectra show a smooth roll-off with increasing frequency and that the scaled spectral shape changes very little across this blockage ratio range.
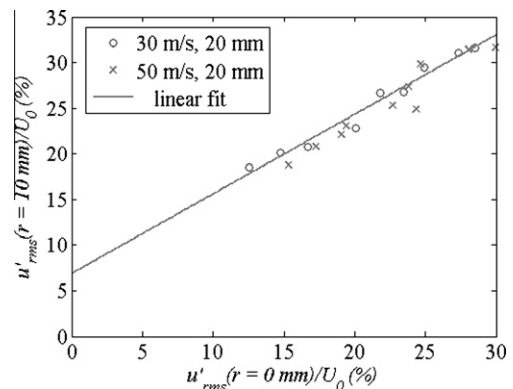

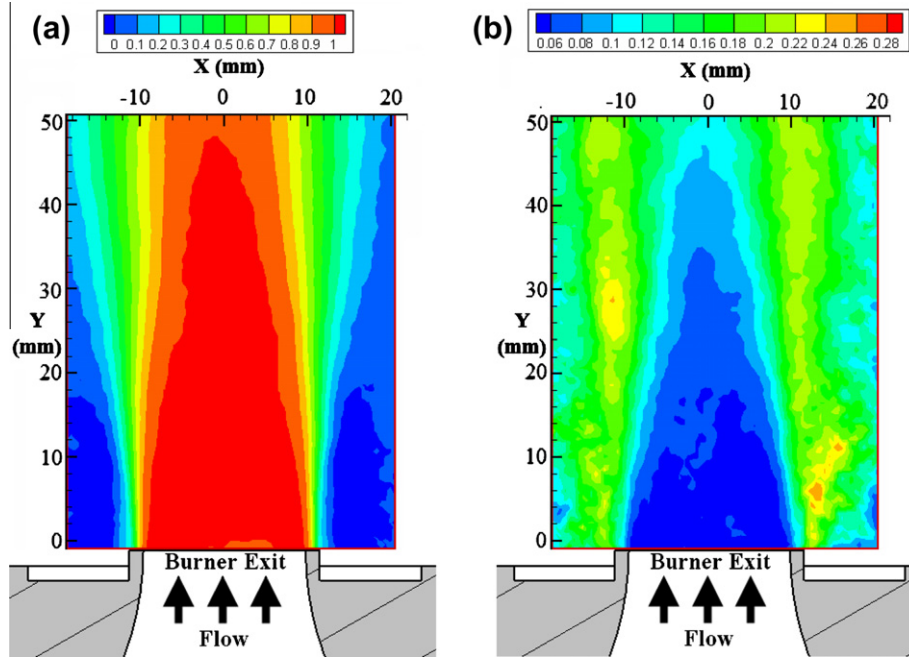**Fig. 8.** Comparison of turbulence intensity in shear layer and burner centerline.

Fig. 9. Cold flow PIV velocity data for the 20 mm burner at a blockage ratio of 80% for U_0 = 4 m/s (a) mean velocity normalized by the centerline mean velocity at the burner exit (b) RMS velocity normalized by the centerline mean velocity at the burner exit.
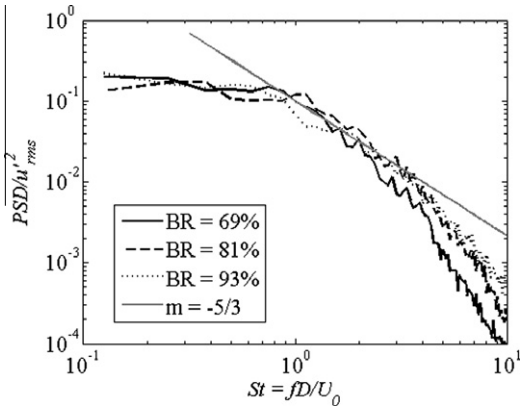

Fig. 10. Turbulent power spectra as a function of Strouhal number, St, for U_0 = 4 m/s at three different blockage ratios.

Integral time scales, t_{int}, were determined from autocorrelations of the centerline LDV velocity data. The autocorrelation function was determined from Eq. (3) using the slotting technique of Mayo [32] with the local normalization improvement described by Tummers and Passchier [33]:

$$\rho(k\Delta\tau) = \frac{\sum_{i=1}^{N-1}\sum_{j=i+1}^{N} u_i u_j(k\Delta\tau)}{\sqrt{\sum_{i=1}^{N-1} u_i^2(k\Delta\tau)\sum_{j=i+1}^{N} u_j^2(k\Delta\tau)}} \qquad (3)$$

where $(k-\frac{1}{2})\Delta\tau < t_i - t_j < (k+\frac{1}{2})\Delta\tau$, $M-1 = \frac{\tau_{max}}{\Delta\tau}$, τ_{max} is the maximum lag time, and $\Delta\tau$ is the slot width. The integral time scale was defined using the relationship:

$$t_{int} = \int_0^\infty \rho(\tau)d\tau \qquad (4)$$

Because of the high uncertainties associated with the autocorrelation at large time lags (because of its low value), an exponential expression of the form $\rho(\tau) = ae^{-b\tau} + (1-a)e^{-c\tau}$ was fit to the autocorrelation function and used to evaluate this integral, so that t_{int} is given by Eq. (5),

$$t_{int} = \frac{a}{b} + \frac{1-a}{c} \qquad (5)$$

A typical result is shown in Fig. 11.

These integral time scales were converted to integral length scales, l_{int}, using the relation $l_{int} = t_{int}U_0$, as per Taylors' hypothesis. Figure 12 summarizes the calculated l_{int}/D values at mean flow velocities of 4, 30, and 50 m/s at various blockage ratios. The data indicate that l_{int}/D is nearly constant at 30 and 50 m/s, and changes slightly with blockage ratio. These data show that turbulence length scales are not varying with blockage gap width and therefore, that the associated variations in turbulence intensity are at essentially constant integral length scale. The t_{int} values in the 4 m/s case are substantially higher in value and do indicate a somewhat higher sensitivity to blockage ratio. It is assumed that this reflects a different characteristic of the turbulence generator system at the much lower Reynolds numbers these data were obtained.
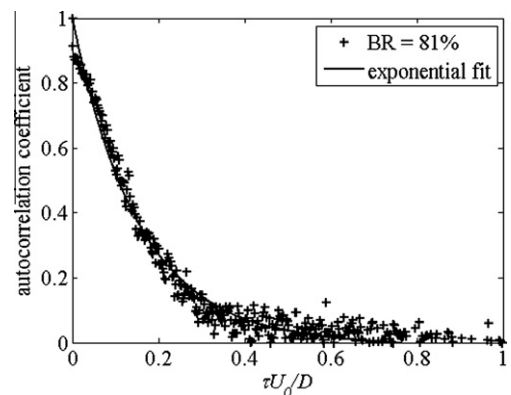

Fig. 11. Autocorrelation coefficient plotted against normalized lag time for U_0 = 4 m/s, blockage ratio = 81%.
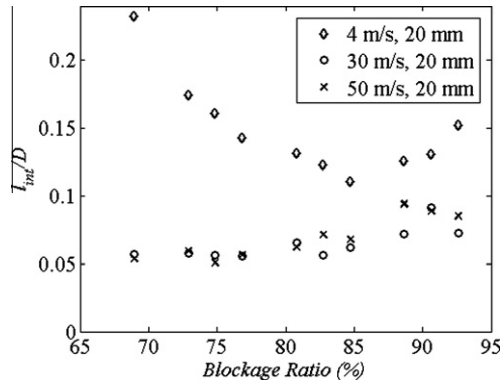
Fig. 12. Comparison of integral length scale (normalized by burner diameter) as a function of blockage ratio at 4, 30 and 50 m/s for the 20 mm burner.

2.2. Image analysis

Global consumption speeds were calculated using Eq. (2), whose key measurement input is progress variable surface area, $\overline{A}_{\langle c \rangle}$. This section describes the approach used to determine this surface area.

Digital images of the flame emission are captured with a 16-bit intensified charge-coupled device (ICCD) camera with a resolution of 512 × 512 pixels and a 105 mm, f/4.5, UV camera lens. The camera system is sensitive in the visible and ultraviolet regions (~220–650 nm) and, hence, is capable of capturing both OH^* and CO_2^* chemiluminescence. This is important for high hydrogen content fuels since the $OH*$ chemiluminescence associated with hydrogen flames emits in the UV range.

Line-of-sight images of the flame were obtained over 5 s and time-averaged; see Fig. 13a. These averaged images are nearly symmetric about the centerline. The left and right halves were then averaged and filtered with a 2-D median filter with a kernel size that is less than 2% of the burner diameter. Note that other potential Bunsen flame $S_{T,GC}$ measurement approaches include Mie scattering [23,34] or OH-PLIF [35] measurements for flame characterization. The resulting progress variable contours (described below) are equivalent for the two methods, assuming that the OH-PLIF or Mie interface surface is equivalent to the chemiluminescence flamelet surface [36,37]. This line-of-sight approach was used here, however, because the OH-PLIF or Mie scattering technique does not capture flame surface density in the out-of-plane direction and, as such, significantly underestimates it. The spatial distribution of heat release is fully captured by a line-of-sight measurement.

To estimate the time-averaged flame brush location from the line-of-sight images, a three-point Abel deconvolution scheme [38] was used; see Fig. 13b. The axial distribution of the centerline intensity is then fit to a Gaussian curve, from which the location of the maximum intensity is identified. This point is associated with the most probable location of the flame, and defined as the $\langle c \rangle = 0.5$ progress variable contour. The estimated uncertainty in identifying this point is 1–2%. The other progress variables were then defined by the following relation:

$$\langle c \rangle = \begin{cases} \frac{I}{I_{max}} & \langle c \rangle \leqslant 0.5 \\ 1 - \frac{I}{I_{max}} & \langle c \rangle > 0.5 \end{cases} \tag{6}$$

Straight lines are then drawn from this point to the two flame anchoring points and rotated about the line of symmetry to generate a cone. The $\langle c \rangle = 0.5$ surface is drawn in Fig. 13b. This method was used to aid in comparing the results of this study with other data in the literature where a similar method was used to determine the flame area (e.g., the "angle method") [7,23,34].

As noted earlier, $S_{T,GC}$ is a function of the progress variable, $\langle c \rangle$, used to define $\overline{A}$. Figure 14 plots the dependence of $S_{T,GC}$ upon the progress variable contour, $\langle c \rangle$, at several H_2/CO ratios, in order to enable comparison of the data in this paper to reported $S_{T,GC}$ data using other progress variable values. As expected, $S_{T,GC}$ decreases with increasing $\langle c \rangle$ value. This graph also shows that the different H_2/CO ratio flames have similar dependence upon $\langle c \rangle$ contour. It also shows that the highest H_2 mixture (90/10 mixture), has the least sensitivity to $\langle c \rangle$, illustrating that the flame brush thickness is decreasing with increased H_2 content.

The overall uncertainty in the estimated $S_{T,GC}$ value is estimated to be 3%.

3. Results and discussion

Two basic sets of tests were performed. Measurements of $S_{T,GC}$ were obtained as a function of $u'/S_{L,0}$ for 12 and 20 mm burner diameters at mean flow velocities from 4 to 50 m/s and volumetric H_2/CO ratios from 30/70 to 90/10, keeping $S_{L,0}$ and reactant temperature fixed at 34 cm/s and 300 K respectively. $S_{L,0}$ was kept nominally constant by adjusting the stoichiometry at each H_2/CO
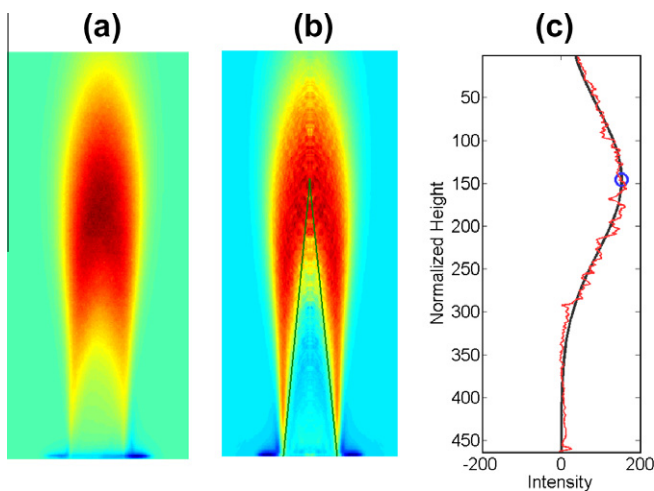

Fig. 13. Time averaged, line-of-sight flame images showing (a) background subtracted image, (b) Abel inverted image with $\langle c \rangle = 0.5$ contour shown, and (c) plot of intensity as a function of image height used to determine contours. The red and black lines represent the raw data and fitted data respectively. (For interpretation of the references to colour in this figure legend, the reader is referred to the web version of this article.)
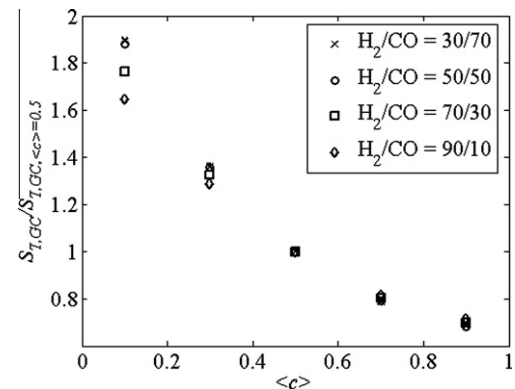

Fig. 14. Dependence of $S_{T,GC}$ value upon using different progress variables normalized by $S_{T,GC},\langle c \rangle = 0.5$ as a function of the progress variable for different H_2/CO ratios at 50 m/s and $u'_{rms}/S_{L,0} = 22.5$, and $S_{L,0} = 0.34$ m/s.

Table 1
Legend used for the constant $S_{L,0}$ data set for the 20 mm burner.

		Velocity (m/s)			
		4	10	30	50
H_2(%)	30	◇	◇	◇	◇
	50	○	○	○	○
	70	◁	◁	◁	◁
	90	✦	✦	✦	✦
CH₄		✚	✚	✚	

Table 2
Legend used for the constant $S_{L,0}$ data set for the 12 mm burner.

		Velocity (m/s)		
		20	30	50
H_2(%)	30	◇	◇	◇
	50		○	
	70		◁	◁
	90	✦	✦	✦

ratio. Additionally, a CH₄/air data set was obtained at the same $S_{L,0}$ (Φ = 0.9). $S_{L,0}$ estimates were determined using the CHEMKIN software [39] with the Davis H₂/CO mechanism for H₂/CO mixtures [40] and GRI 3.0 for CH₄/air [41]. Symbol type and color scheme are summarized in Tables 1 and 2.

The second set of tests was performed by sweeping the equivalence ratio at constant H₂/CO ratio values of 30/70 and 60/40 with the 20 mm burner. The symbol type and color scheme used for this data set are summarized in Table 3.

The parameter ranges explored in this study are summarized in Table 4. Figure 15 summarizes where the measured data is located on a Borghi diagram [42] for the 12 and 20 mm burner diameters.

Flame speed stretch sensitivities were also calculated using an opposed flow calculation of two premixed flames with a nozzle separation distance of 20 mm, using the OPPDIF module in CHEMKIN. These calculations were used to extract various properties of the strained flame characteristics. The stretched flame speed, S_L, reported here is defined as the minimum velocity just ahead of the reaction zone, as suggested by Wu and Law [43]. The Markstein length, l_M, was determined from the slope of the linear fit in the
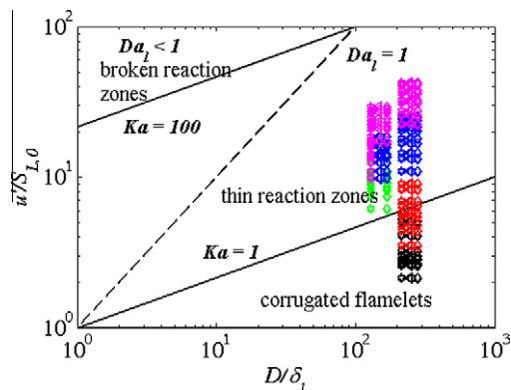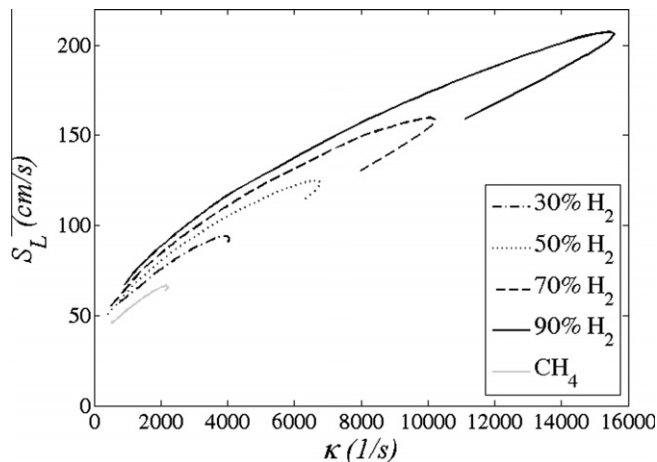
Table 3
Legend for constant H₂ content equivalence ratio sweeps data for the 20 mm burner.

		Velocity (m/s)			
H_2	Φ	4	10	30	50
30	0.61	★	★	★	★
	0.7	✱	✱	✱	✱
	0.8	▽	▽	▽	▽
60	0.4	▷	▷	▷	▷
	0.6	✖	✖	✖	✖
	0.8	□	□	□	□

Table 4
Investigated parameter space.

	Constant. $S_{L,0}$				ϕ sweep					CH₄
U_o (m/s)	4, 10, 30, 50									4, 10, 30
H_2 (%)	30	50	70	90	30		60			0
ϕ	0.61	0.55	0.51	0.48	0.7	0.8	0.4	0.6	0.8	0.9
$S_{L,0}$ (m/s)	0.34				0.48	0.59	0.15	0.51	0.9	0.34

Fig. 15. Borghi diagram showing location of constant $S_{L,0}$ study data points for the 12 and 20 mm burners.

Fig. 16. Stretch sensitivity calculations of constant $S_{L,0}$ mixtures (see Table 4 for stoichiometry values of each mixture).

low strain regime of the κ vs. S_L curve. Extinction strain rates, κ_{ext} were calculated using an arc length continuation method [44]. An example set of calculations for the constant $S_{L,0}$ mixtures are show in Fig. 16, showing that the mixtures converge to the same $S_{L,0}$ at κ = 0. However, they clearly have different stretch sensitivities as quantified by the Markstein length and extinction strain rates. These stretch sensitivities are used later in the flame speed correlation section to facilitate analysis of these data.

3.1. H₂/CO sweeps at constant $S_{L,0}$

This section presents data for various H₂/CO ratios at nominally constant $S_{L,0}$. Figures 17 and 18 plots $S_{T,GC}/S_{L,0}$ for H₂/CO mixtures of 30/70, 50/50, 70/30, and 90/10 at mean flow velocities of 4, 10, 30, and 50 m/s for the 20 mm burner. These two graphs plot the same data on a linear (Fig. 17) and log (Fig. 18) scale. As expected, $S_{T,GC}$ increases monotonically with turbulence intensity, for a given fuel composition. The data also clearly indicate the monotonically
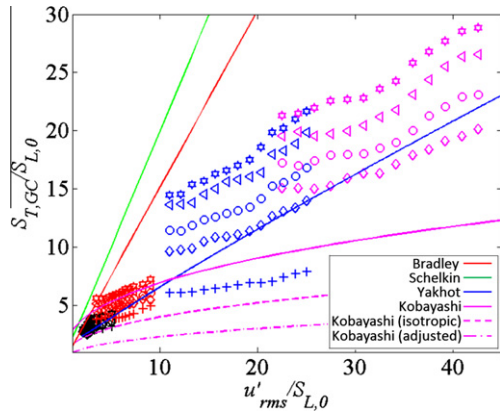
Fig. 17. Linear plot of variations of turbulent flame speed, $S_{T,GC}$, with turbulence intensity, u'_{rms}, normalized by $S_{L,0}$ at various mean flow velocities and H_2/CO ratios for the 20 mm burner (see Table 1 for legend of mixture conditions and flow velocities).
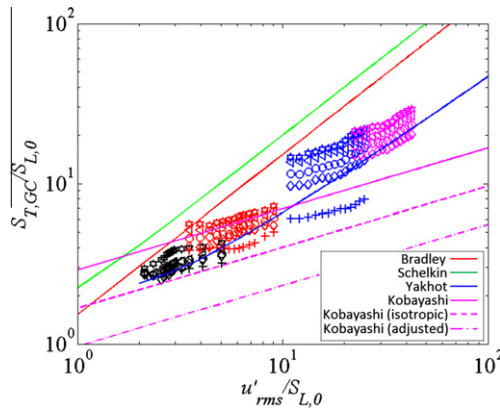

Fig. 18. Log–log plot of variations of turbulent flame speed, $S_{T,GC}$, with turbulence intensity, u'_{rms}, normalized by $S_{L,0}$ at various mean flow velocities and H_2/CO ratios for the 20 mm burner (see Table 1 for legend of mixture conditions and flow velocities).

increasing value of $S_{T,GC}$ with H_2 levels. For example, at $U_0 = 30$ m/s and $u'_{rms}/S_{L,0} = 25$, $S_{T,GC}/S_{L,0}$ has a value of 8 for CH_4, of 14 for the 30/70 H_2/CO mix and 22 for the 90/10 H_2/CO mix. Moreover, the data indicate that these "fuel effects" persist even at very high turbulence intensities. Note also the significant similarities between each fixed mean flow velocity group as fuel composition is varied. It appears that the same curve is shifted vertically to higher $S_{T,GC}$ values as H_2 fraction is increased.

Also included on these graphs for reference are several measured or predicted S_T correlations (discussed further in Appendix A). Some caution should be exercised in comparing these with the data, because of the definition dependence of S_T and u'_{rms} noted earlier. Although many of these are local consumption speed based correlations, they do reasonably bracket the results.

The data for the 12 mm burner at various H_2/CO ratios at nominally constant $S_{L,0}$ are summarized in Fig. 19 which plot $S_{T,GC}/S_{L,0}$ for H_2/CO blends at mean flow velocities of 20, 30, and 50 m/s.

Note that larger average consumption speeds are seen with the larger burner diameter, at a given fuel composition, turbulence intensity, and mean flow velocity. These differences are about 50% for 50 m/s and 60% for 30 m/s. This shows the well known length scale sensitivity of the turbulent flame speed [4].

Although not the primary focus of this study, the mean flow dependencies at a given fuel composition are worthy of mention. First, these data clearly show the well known dependence of $S_{T,GC}$ upon U_0, a fact highlighted in other studies [5,11]. Each velocity
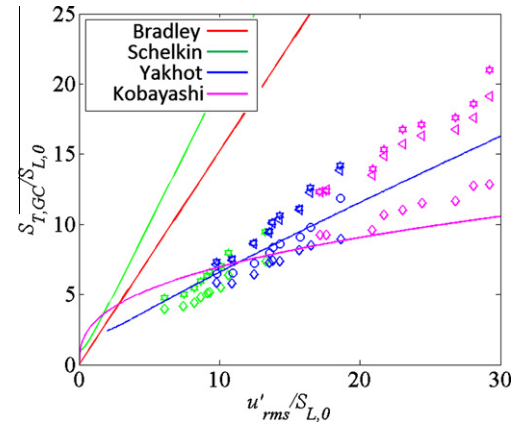

Fig. 19. Variations of turbulent flame speed, $S_{T,GC}$, with turbulence intensity, u'_{rms}, normalized by $S_{L,0}$ at various mean flow velocities and H_2/CO ratios for the 12 mm burner (see Table 2 for legend of mixture conditions and flow velocities).

result appears to lie on a separate curve, which is roughly parallel to the other velocity results, but does not intersect it at the same turbulence intensity. For example, $S_{T,GC}/S_{L,0}$ differs by 100% at $U_0 = 10$ and 30 m/s, for the 90% H_2 mixture at $u'_{rms}/S_{L,0} = 10$. As a second example, $S_{T,GC}/S_{L,0}$ differs by 36% between the $U_0 = 4$ and 10 m/s cases, at $u'_{rms}/S_{L,0} = 5$ for the 90% H_2 mixture. This mean flow dependence is less obvious between the $U_0 = 30$ and 50 m/s cases, presumably because the fractional variation in U_0 is smaller here than in the other cases.

3.2. Equivalence ratio sweeps at constant H_2 content

In order to determine the effect of varying $S_{L,0}$ at fixed H_2 fractions, equivalence ratio sweeps were also performed at fixed H_2 contents of 30% and 60% for three equivalence ratios using the 20 mm burner diameter. The symbols used for Figs. 20–23 are presented in Table 3. Figures 20 and 21 show the results for a 60% H_2 mixture at $\phi = 0.4, 0.6, 0.8$ for mean flow velocities of 4, 10, 30, and 50 m/s. Note that $S_{L,0}$ is not constant for these data, as it was in the prior section.

As in Figs. 17–19, the S_T correlations discussed in Appendix A have also been plotted. From Fig. 21, which is the log–log version of Fig. 20, it is seen that the data generally fall within the band formed by the correlations given by Eqs. (A1) and (A3). Furthermore, the slope of the data seems to agree quite well with Kobay-
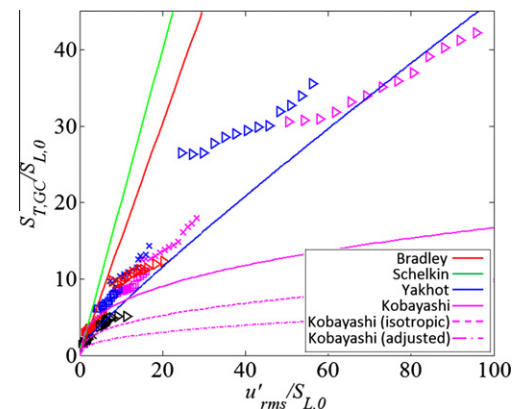

Fig. 20. Linear plot of variations of the turbulent flame speed, $S_{T,GC}$, with turbulence intensity u'_{rms} normalized by $S_{L,0}$ at various mean flow velocities and equivalence ratios at a fixed H_2 content of 60% for the 20 mm burner (see Table 3 for legend of mixture conditions and flow velocities).
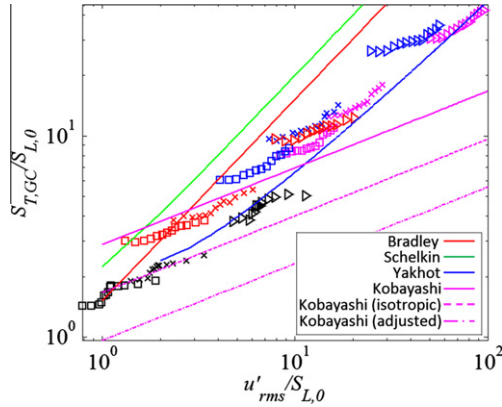
Fig. 21. Log–log plot of variations of the turbulent flame speed, $S_{T,GC}$, with turbulence intensity u'_{rms} normalized by $S_{L,0}$ at various mean flow velocities and equivalence ratios at a fixed H_2 content of 60% for the 20 mm burner (see Table 3 for legend of mixture conditions and flow velocities).

Fig. 22. Linear plot of variations of the turbulent flame speed, $S_{T,GC}$, with turbulence intensity u'_{rms} normalized by $S_{L,0}$ at various mean flow velocities and equivalence ratios at a fixed H_2 content of 30% for the 20 mm burner (see Table 3 for legend of mixture conditions and flow velocities).
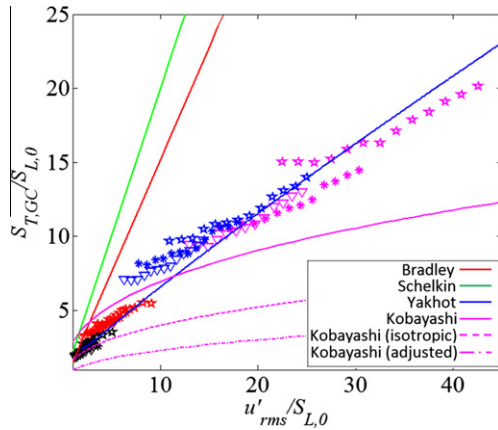

Fig. 23. Log–log plot of variations of the turbulent flame speed, $S_{T,GC}$ with turbulence intensity u'_{rms} normalized by $S_{L,0}$ at various mean flow velocities and equivalence ratios at a fixed H_2 content of 30% for the 20 mm burner (see Table 3 for legend of mixture conditions and flow velocities).
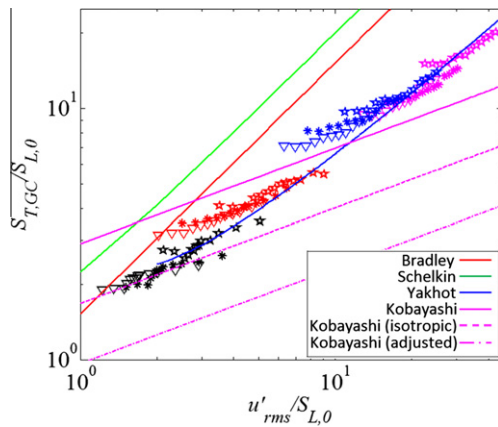
ashi's correlation, given by Eq. (A4), particularly at the low to intermediate $u'_{rms}/S_{L,0}$ ranges.

Figures 22 and 23 shows the results for a 30% H_2 mixture at ϕ = 0.61, 0.7, 0.8 for mean flow velocities of 4, 10, 30, and 50 m/s. Similar conclusions can be reached from this data as discussed above.

Again from Fig. 23, which is the log–log version of Fig. 22, it can be seen that the data generally fall within the band created by the Eq. (A1) and Eq. (A3). Furthermore, since the $u'_{rms}/S_{L,0}$ range investigated with the 30/70 H_2/CO mixture is smaller, it is easier to see that correlation given by Eq. (A3) is a close match.

4. Analysis of flame speed data

These data are consistent with prior studies showing that stretch sensitivity of the reactants has an important impact on the turbulent flame speed [3,11]. This point is shown in Fig. 24, which plots the dependence of these data upon calculated Markstein length of the reactants, l_M (see Fig. 16), at two different turbulence intensities for the constant $S_{L,0}$ studies. The point located at $l_M = -0.02$ for $u'_{rms}/S_{L,0} = 20$ corresponds to the methane–air mixture at ϕ = 0.9. Note the monotonically increasing value of $S_{T,GC}$ with $|l_M|$. The difference in flame speeds between low and high H_2 flames for the H_2/CO blends and the CH_4/air and H_2/CO/air flames is significant, being as large as two and three, respectively.

A common approach for scaling turbulent flame speeds is to use the consumption based definition [11]:

$$S_T = \frac{\langle S_L A \rangle}{A_0} \qquad (7)$$

Or, by introducing the stretch factor, $I_0 = S_L/S_{L,0}$ [45,46]:

$$S_T = \frac{S_{L,0} \langle I_0 A \rangle}{A_0} \qquad (8)$$

For stretch insensitive flames, the I_0 factor equals unity, leading to the classical S_T scaling described by Damköhler [47]. For stretch sensitive flames, one is left with the function $\langle I_0 A \rangle$, which requires understanding the correlation between local flame speed and flame area. Assuming that these functions are uncorrelated, i.e., that $\langle I_0 A \rangle = \langle I_0 \rangle \langle A \rangle$ leads to the erroneous prediction that the mixture's stretch sensitivity should not influence S_T [48]. This prediction follows from measurements and computations which show that the flame curvature PDF is roughly symmetric about $\kappa = 0$ [49–52], implying that regions of enhanced and diminished local consumption rate should roughly cancel and, thus, that $\langle I_0 \rangle \approx 1$. Hydrodynamic strain, which is not symmetric about $\kappa = 0$ [51–53] does introduce a non-unity $\langle I_0 \rangle$ value, but it seems unlikely that this effect is significant enough to explain the appreciable fuel effects reported here and in the literature.
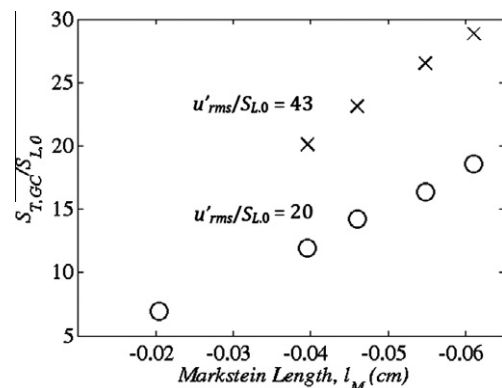

Fig. 24. Dependence of $S_{T,GC}/S_{L,0}$ upon Markstein length, l_M, for $u'_{rms}/S_{L,0}$ = 20 and 43 at $S_{L,0}$ = 0.34 m/s.

However, it can easily be seen that assuming uncorrelated A and I_0 passes over key physics: in particular, there are implicit I_0 effects in the $\langle A \rangle$ term because the local flame speed and area are highly correlated. For example, if the positively curved leading point of the flame has a higher local flame speed, it will propagate at a faster speed into the unburned reactants, increasing flame area accordingly. In the same way, the slower, negatively curved trailing point of the flame will lag backwards, also increasing flame area.

Given the implicit presence of the I_0 term in the $\langle A \rangle$ term, modeling approaches based upon leading points concepts [3,8,22] may be more useful for explicitly bringing out stretch sensitivity effects. The leading points are roughly defined as the necessarily positively curved points on the turbulent flame front that propagate farthest into the reactants. It has been argued that the propagation speed of these points with respect to the average flow velocity control the overall turbulent flame speed [22]. As a result, fuel/air mixtures with negative Markstein numbers will have enhanced laminar flame speeds at the positively curved leading points, resulting in larger displacement speeds.

This basic leading points argument can be readily understood from the simple model problem of a flat flame propagating into a spatially varying velocity field with zero mean flow velocity, as depicted in Fig. 25.

If we assume that S_L remains constant, then it is seen that the portion of the flame at the lowest velocity point propagates out the fastest. In the lab-fixed coordinate system, the flame at Point B moves at a speed of $S_L + (\Delta u)_{LP}$, where the subscript "LP" denotes the leading point. Moreover, it can easily be shown by a front tracking computation that, after an initial transient, the entire front reaches a stationary shape and propagation speed with the value $S_L + (\Delta u)_{LP}$ as shown in Fig. 26. As such, the overall displacement speed is controlled by the leading points of the flame that propagate into the lowest velocity regions ahead of the flame. Note also that the flame area would increase as well, but this is an *effect* of the higher displacement speed, not the *cause*.

In reality, the positively curved leading point of the flame will have an altered flame speed, $(S_L)_{LP} = S_{L,0} + (S_L')_{LP}$, where $(S_L')_{LP}$ is the modification of the un-stretched laminar flame speed at the leading point, because of the mixtures non-zero Markstein length. If the mixture has a negative Markstein number, then the flame

speed at this point will further increase, causing an increase in curvature, further increasing the local flame speed. This is, in essence, a restatement of the fact that such negative Markstein length mixtures are thermo-diffusively unstable [12]. As a result, the above expression can be modified to take into account the flame speed augmentation:

$$S_D = S_{L,0} + (S_L')_{LP} + (\Delta u)_{LP} \qquad (9)$$

The key difference to note from this scaling approach relative to Eq. (2) is that this focuses on a local flame characteristic – namely the positively curved leading point – as opposed to some global average, $\langle I_0 A \rangle$, which obscures the stretch effect.

The key problem lies in scaling $(S_L')_{LP}$. If the positively curved leading point is weakly stretched, then $(S_L')_{LP} \sim l_M \kappa_{LP}$. This switches the problem to scaling the strain statistics conditioned on the leading point of the flame, κ_{LP}, an important fundamental problem in turbulent combustion; see Lipatnikov and Chomiak [3] for discussion. However, the properties of negative Markstein number fuels can be utilized to place a bound on $(S_L')_{LP}$. Since the investigated mixtures are thermo-diffusively unstable, the $\kappa = 0$, $S_L = S_{L,0}$ point is 'repelling' points in flame strain rate space. In other words, any perturbation of a flat flame will grow, causing an increase in curvature of the positively curved leading edge of the flame. This increase in curvature causes a further increase in flame speed and, therefore, a further increase in curvature, see Fig. 27. In fact, as will be shown more rigorously in the subsequent discussion, $S_L = S_{L,max}$ is a steady-state 'attracting' point for a positively curved wrinkle. Moreover, the flame speed at the leading point, $(S_L)_{LP}$ is bounded by the $S_{L,max}$ value; i.e., $S_{L,max} > (S_L)_{LP} > S_{L,0}$. For an opposed flow flame, $S_{L,max}$ can be directly extracted from the simulations shown in Fig. 16. For example, this leads to the following inequality for the 30% H_2 blend: 95 cm/s > $(S_L)_{LP}$ > 34 cm/s.

Substituting $S_{L,max}$ in for $(S_L)_{LP}$ and writing $(\Delta u)_{LP}$ as u'_{LP}, leads to the following:

$$\frac{S_D}{S_{L,max}} \leqslant 1 + \frac{u'_{LP}}{S_{L,max}} \qquad (10)$$

Note that this is similar to Damköhler's classical result [47] where S_L has been replaced by $S_{L,max}$ and u' by u'_{LP}.

On the basis of the scaling derived above, all the $S_{T,GC}$ data presented above are replotted in Fig. 28 using the $S_{L,max}$ normalization. Because of the mean flow dependencies noted earlier, we first plot this data first at fixed flow velocities.

Figure 28 shows that the data collapses generally well across all the mean flow velocities. There is some scatter that in the 4 m/s data that largely disappears at the higher flow velocities. Also, note that the 30 m/s CH_4/air data does not collapse with the H_2/CO data set, while it collapses at 10 m/s and 4 m/s.
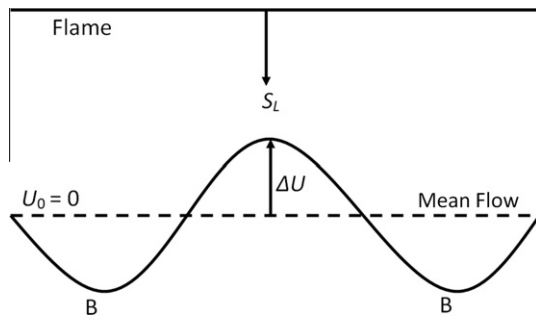
Fig. 25. Model problem of a flat flame propagating into a spatially varying flow field.
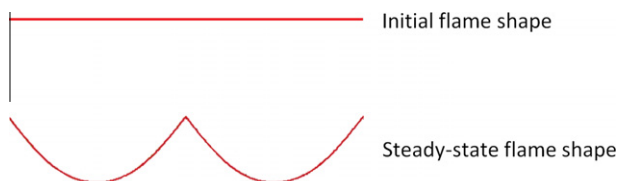
Fig. 26. Level set computation of model problem shown in Fig. 25, where the initial and final steady-state flame shapes are shown.
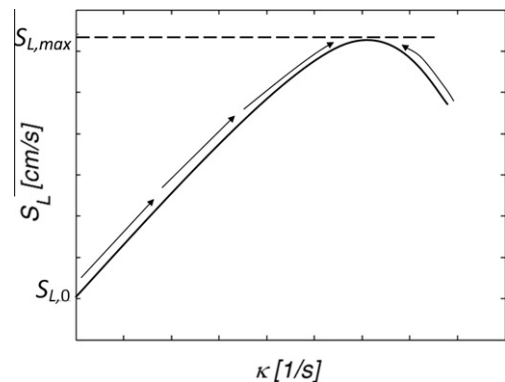
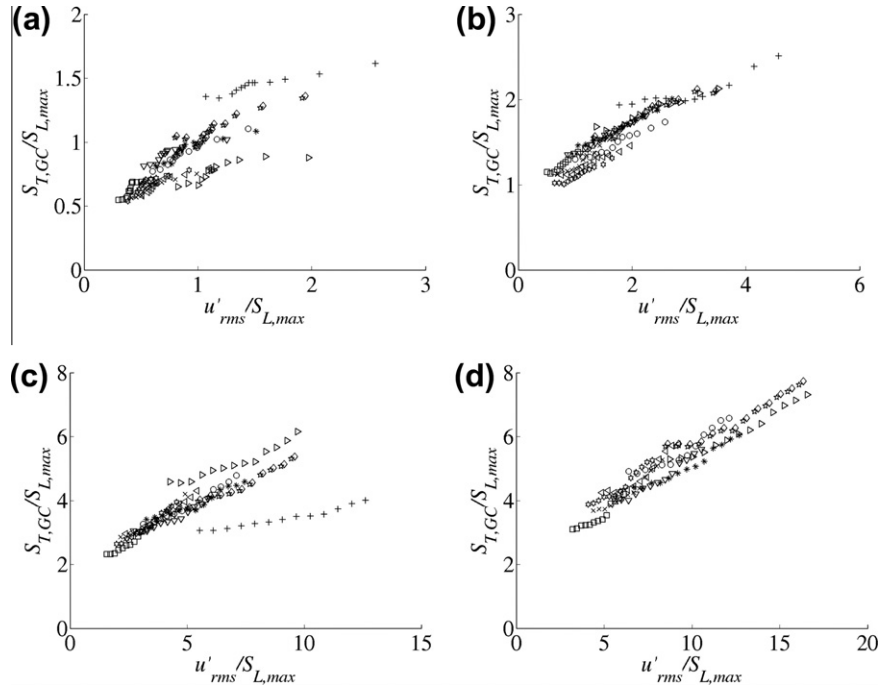**Fig. 27.** Example plot showing the 'attracting' nature of $S_{L,max}$.

Fig. 28. Variations of the turbulent flame speed, $S_{T,GC}$, with turbulence intensity u'_{rms} normalized by $S_{L,max}$ of both constant $S_{L,0}$ and equivalence ratio sweep studies for 20 mm burner grouped by mean flow velocities (a) 4 m/s (b) 10 m/s (c) 30 m/s (d) 50 m/s (see Tables 1 and 3 for legend).

Figure 29 plots the entire 20 mm burner data set, which contains both the constant $S_{L,0}$ studies and the equivalence ratio sweep studies, while Fig. 30 displays the renormalized 12 mm burner data.

From Figs. 29 and 30 it is clear that both data sets collapse very well, with the exception of the 30 m/s CH$_4$ data. In fact for the
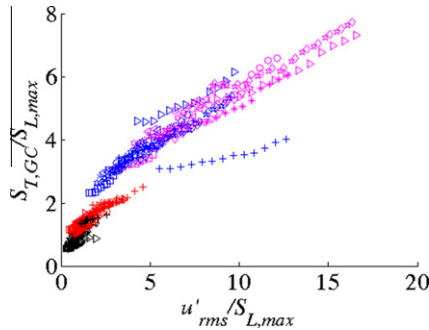

Fig. 29. $S_{L,max}$ normalized $S_{T,GC}$ data for the 20 mm burner including constant $S_{L,0}$ and equivalence ratio sweep studies (see Tables 1 and 3 for legend).
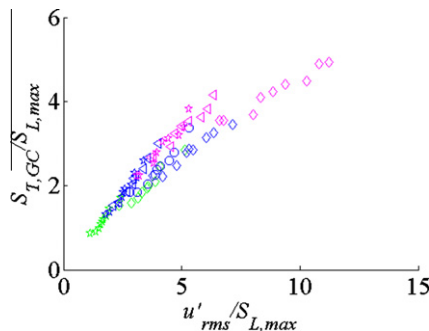

Fig. 30. $S_{L,max}$ normalized $S_{T,GC}$ data for the 12 mm burner for constant $S_{L,0}$ studies (see Table 2 for legend).

20 mm constant $S_{L,0}$ data set, the variation in the normalized turbulent flame speed values for the 30/70 to 90/10 reduced from 50% to about 10% (for the 50 m/s case) between Figs. 17 and 29. Larger disparities (about 50% at $u'_{rms}/S_{L,max} = 12.5$) are seen between the H$_2$/CO data and CH$_4$ data. This scatter and some caveats are discussed further in the following paragraphs.

First, some scatter is inevitable as the κ_{ext} and $S_{L,max}$ value are not constants for a given mixture but depends upon the strain profile the flame is subjected to [54] and the relative amount of curvature versus hydrodynamic induced flame stretch. For example, repeating these calculations using nozzle separation distances ranging from 10 to 40 mm causes variations in $S_{L,max}$ of 5% for the 30/70 H$_2$/CO mixture. Moreover, this $S_{L,max}$ value is a function of the experimental configuration – in the opposed flow configuration, it is closely related to reaction zone impingement on the stagnation plane so that complete reaction is not possible [12]. Presumably, the $S_{L,max}$ at the leading point of the turbulent flame brush would be related to the strain rate associated with the highly curved leading edge, whose radius of curvature is bounded by the flame thickness.

Second, the local burning velocity at the leading point, $(S_L)_{LP}$ is not identically equal to $S_{L,max}$; rather, $S_{L,max}$ is simply an upper bound of an inequality. The reason that the $S_{L,max}$ correlation appears to work well is that $S_L = S_{L,max}$ is an attracting point. Thus, in the "quasi-steady" limit where the turbulence evolves slowly relative to the time scale over which the leading point of the flame can respond, $(S_L)_{LP}$ must always tend toward $S_{L,max}$. This point was made heuristically above, but it can also be shown formally by considering the following level set equation describing the flame's spatio-temporal dynamics,

$$\frac{\partial G}{\partial t} + \vec{u} \cdot \vec{\nabla} G = S_L |\vec{\nabla} G| \tag{11}$$

This is a suitable model for the flame's dynamics, as Fig. 15 shows that the data falls primarily in the corrugated flamelets and thin reaction zone regimes. This equation can be treated

analytically in the low turbulence intensity limit, where the flame position is a single-valued function of some coordinate $G = y - \xi(x, t)$, as shown in Fig. 31.

Writing the stretch sensitive flame speed as $S_L = S_{L,0}[1 + f(\kappa)]$, we obtain:

$$-\frac{\partial \xi}{\partial t} - U\frac{\partial \xi}{\partial x} + V = S_{L,0}[1 + f(\kappa)]\left[1 + \left(\frac{\partial \xi}{\partial x}\right)^2\right]^{1/2} \tag{12}$$

Differentiating this expression with respect to x, and substituting $g = \partial \xi/\partial x$:

$$-\frac{\partial g}{\partial t} - \frac{\partial}{\partial x}(Ug) + \frac{\partial V}{\partial x} = S_{L,0}(1 + g^2)^{1/2}\frac{\partial f}{\partial \kappa}\frac{\partial \kappa}{\partial x} + S_{L,0}[1 + f(\kappa)]$$
$$\times \frac{g}{(1 + g^2)^{1/2}}\frac{\partial g}{\partial x} \tag{13}$$

A necessary condition for leading points, located at the points, x_{LP}, is that $g(x_{LP}, t) = 0$ and $\partial g(x_{LP}, t)/\partial x < 0$. We can determine the asymptotic tendencies of these leading points in a quiescent medium by taking the steady-state limit of this equation by setting $\partial g/\partial t = 0$ and $U = V = 0$. Furthermore, by explicitly writing the curvature induced strain, κ, as $\frac{\partial g/\partial x}{(1+g^2)^{3-2}}$, Eq. (13) can then be expressed as:

$$0 = S_{L,0}(1 + g_{ss}^2)^{1/2}$$
$$\times \frac{\partial f}{\partial \kappa}\left[\frac{\partial^2 g_{ss}}{\partial x^2}(1 + g_{ss}^2)^{-3/2} - 3g_{ss}(1 + g_{ss}^2)^{-5/2}\left(\frac{\partial g_{ss}}{\partial x}\right)^2\right]$$
$$+ S_{L,0}[1 + f(\kappa)]\frac{g_{ss}}{(1 + g_{ss}^2)^{1/2}}\frac{\partial g_{ss}}{\partial x} \tag{14}$$

Setting $g_{ss} = 0$ shows that the following necessary condition is satisfied at the leading point:

$$\frac{\partial f}{\partial \kappa}\frac{\partial^2 g_{ss}}{\partial x^2} = 0 \tag{15}$$

Eq. (15) shows that the steady-state leading points must occur where $\partial f/\partial \kappa = 0$, which coincides with the location of $S_L = S_{L,max}$. Physical arguments can also be used to show that this is a stable attracting point if $\partial^2 f/\partial \kappa^2 < 0$, and that $\partial g/\partial x < 0$ at this $\partial f/\partial \kappa = 0$ point.

The above analysis clearly shows that equating $(S_L)_{LP}$ with $S_{L,max}$ is appropriate in the "quasi-steady" limit of slow turbulent fluctuations. In reality, the leading points continuously evolve in time, as the character of the turbulent fluctuations change, causing points to move and the leading points at a given instant approximately corresponding to the points of local minimum in velocity. Further analysis is needed to understand these unsteady effects and how they influence $(S_L)_{LP}$ scaling.

Finally, note that the $S_{T,GC}$ data reported here by virtue of Eq. (2) necessarily average over potentially significant variations in local flame speeds whereas the scaling shown in Eq. (10) is essentially valid at a single point on the instantaneous flame front. As a result, adjustments to suitably average over a spatially developing flow

Fig. 31. Coordinate system defining the instantaneous flame location, $\xi(x, t)$.

field and flame brush are required. Nonetheless, the very good collapse of the large data set obtained here provides strong evidence for the basic validity of the scaling argument shown in Eq. (10). Note that this argument will need revisiting for $l_M > 0$ flames, where the attracting point argument discussed above requires modification.

5. Concluding remarks

The data presented in this paper clearly corroborate results from other studies showing significant sensitivity of $S_{T,GC}$ to fuel composition over a wide range of turbulence intensities. For example, $S_{T,GC}$ in the 90% H_2 case is three times larger than the CH_4 mixture with the same $S_{L,0}$ value. An important conclusion from this work is that fuel effects on $S_{T,GC}$ highlighted above are not simply a low turbulence intensity phenomenon – they clearly persist over the entire range of turbulence intensities used in the measurements.

It is believed that these fuel effects are due to the reactant mixture stretch sensitivity, which has a strong effect on the positively strained leading points of the turbulent flame brush for non-zero Markstein length fuels. These leading points propagate at a rate equal to the turbulent displacement speed. We showed that leading point concepts lead to a scaling law that collapses much of the data. Furthermore, modeling the instantaneous flame front using the G-equation, we were also able to show that the flame speed at the leading point always tends towards $S_{L,max}$ in a quasi-steady flow, validating the choice of $S_{L,max}$ as parameter to correlate the $S_{T,GC}$ data. However, additional work is needed to develop better scaling rules for the flame strain characteristics at the leading point, κ_{LP}, as well as to develop suitable averaging procedures to capture spatial variations in turbulent consumption speed that are present in the global consumption speed.

Appendix A:. Explanation of other correlations

Bradley's equation [55] is given by:

$$\frac{S_T}{S_L} = 1.52\frac{u'}{S_L} \tag{A1}$$

This is a theoretical result derived from considerations of the fractal characteristics of high intensity turbulent flames. It was derived using theoretically and experimentally obtained values for the fractal dimension and turbulent dissipation coefficients. As a result, the analysis appears to lend itself to a local definition of turbulent flame speed such as $S_{T,LC}$ or $S_{T,LD}$. A similar expression, derived from a different theoretical approach, was proposed by Anand and Pope [56], with a constant of 1.5.

Schelkin's expression [57] is given by:

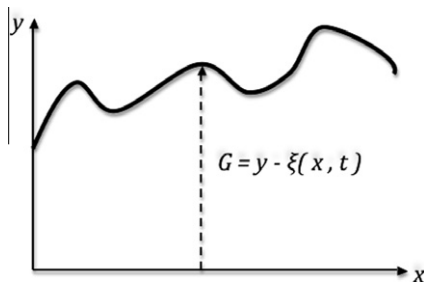$$\frac{S_T}{S_L} = [1 + (2\frac{u'}{S_L})^2]^{0.5} \tag{A2}$$

This is also a theoretical result that most closely corresponds to $S_{T,LC}$ or $S_{T,LD}$ using Damköhler's approach to wrinkled flames where the turbulent structures are much larger than the laminar flame thickness [58].

Yakhot [59] also developed the following theoretical expression, valid again for high turbulence intensity flames using group renormalization approaches. Again, this expression most closely corresponds to $S_{T,LC}$ or $S_{T,LD}$.

$$\frac{S_T}{S_L} = \exp\left[\left(\frac{S_T}{S_L}\right)^2 \bigg/ \left(\frac{u'}{S_L}\right)^2\right] \tag{A3}$$

Kobayashi [27] developed a correlation from experimental data for CH_4/air and C_2H_4/air turbulent Bunsen flames that included pressure effects.

$$\frac{S_T}{S_L} = 2.9\left[\left(\frac{P}{P_0}\right)\left(\frac{u'}{S_L}\right)\right]^{0.38} \tag{A4}$$

This value of S_T was based upon the $\langle c \rangle = 0.5$ contour and corresponds to the global consumption speed definition. Figures 17 and 18 show that the correlation over-predicts $S_{T,GC}$ for our CH_4/air data, but generally follows the observed trend. One possibility for this is that the turbulence intensity quoted by Kobayashi et al. [23] is only the axial RMS, while turbulence intensity used in the current study is the total RMS which includes axial as well as radial and azimuthal components. Under the assumption that the turbulence intensity quoted by Kobayashi only included axial RMS fluctuations and assuming they had isotropic turbulence, their correlation was adjusted to include all three components of the RMS fluctuations. This new curve fit is labeled "Kobayashi (isotropic)" in Figs. 17 and 18. In order to examine this effect further, the relationship between our measured axial RMS and total RMS was found to be $u' = u'_{rms}/3$. This relationship was then used to again adjust the turbulence intensity values reported by Kobayashi. This curve is labeled "Kobayashi (adjusted)". As shown in Figs. 17 and 18, both of the adjusted correlations under-predict the values found, however, the original correlation of Kobayashi and the one adjusted for isotropic turbulence bracket the CH_4 values obtained in this experiment.

References

[1] G.A. Richards, K.H. Casleton, in: T.C. Lieuwen, V. Yang, R.A. Yetter (Eds.), Synthesis Gas Combustion: Fundamentals and Applications, CRC Press, 2009, p. 403.
[2] T. Lieuwen, V. McDonell, E. Petersen, D. Santavicca, J. Eng. Gas Turbines Power 130 (2008). 011506-1–011506-10.
[3] A.N. Lipatnikov, J. Chomiak, Prog. Energy Combust. Sci. 31 (1) (2005) 1–73.
[4] A.N. Lipatnikov, J. Chomiak, Prog. Energy Combust. Sci. 28 (1) (2002) 1–74.
[5] S.A. Filatyev, J.F. Driscoll, C.D. Carter, J.M. Donbar, Combust. Flame 141 (2005) 1–21.
[6] D.R. Ballal, A.H. Lefebvre, Acta Astronaut. 1 (3–4) (1973) 471–483.
[7] D. Ballal, A. Lefebvre, Proc. R. Soc. London A: Math. Phys. Sci. 344 (1637) (1975) 217–234.
[8] V.R. Kuznetsov, V.A. Sabel'nikov, in: V.R. Kuznetsov, V.A. Sabel'nikov, P.A. Libby (Eds.), Turbulence and Combustion, Hemisphere Publishing Corporation, Moscow, 1986, p. 362.
[9] M. Nakahara, H. Kido, AIAA J. 46 (7) (2008) 1569–1575.
[10] H. Kido, M. Nakahara, K. Nakashima, J. Hashimoto, Proc. Combust. Inst. 29 (2) (2002) 1855–1861.
[11] J.F. Driscoll, Prog. Energy Combust. Sci. 34 (1) (2008) 91–134.
[12] C.K. Law, Combustion Physics, Cambridge University Press, New York, 2006.
[13] S. Daniele, P. Jansohn, K. Boulouchos, in: Proceedings of ASME Turbo Expo 2009, GT 2009-59477, Orlando, Florida, 2009.
[14] S. Daniele, P. Jansohn, J. Manzaras, K. Boulouchos, Proc.Combust.Inst. 33 (2) (2011) 2937–2944.
[15] V.P. Karpov, E.S. Severin, Combust. Explo. Shock Waves 18 (6) (1982) 643–644.
[16] M.S. Wu, S. Kwon, J.F. Driscoll, G.M. Faeth, Combust. Sci. Technol. 73 (1) (1990) 327–350.
[17] Ö.L. Gülder, G.J. Smallwood, R. Wong, D.R. Snelling, R. Smith, B.M. Deschamps, J.C. Sautet, Combust. Flame 120 (4) (2000) 407–416.
[18] T. Kitagawa, T. Nakahara, K. Maruyama, K. Kado, A. Hayakawa, S. Kobayashi, Int. J. Hydrogen Energy 33 (20) (2008) 5842–5849.
[19] H. Kido, M. Nakahara, J. Hashimoto, D. Barat, JSME Int. J. Ser. B: Fluids Therm. Eng. 45 (2) (2002) 355–362.
[20] A. Betev, V. Karpov, E. Semenov, Chemical Physics Reports C/C of Khimicheskaia Fizika, vol. 16, 1997, pp. 1861–1868.
[21] H. Kobayashi, Y. Kawabata, K. Maruta, Proc. Combust. Inst. 27 (1998) 941–948.
[22] V.P. Karpov, A.N. Lipatnikov, V.L. Zimont, in: Ya.B. Zel'dovich, W.A. Sirignano, A.G. Merzhanov, L. De Luca (Eds.), Advances in Combustion Science, vol. 173, AIAA, Reston, VA, 1997, pp. 235–250.
[23] H. Kobayashi, T. Tamura, K. Maruta, T. Niioka, F.A. Williams, Proc. Combust. Inst. 26 (1996) 389–396.
[24] R.K. Cheng, in: T.C. Lieuwen, V. Yang, R.A. Yetter (Eds.), Synthesis Gas Combustion: Fundamentals and Applications, CRC Press, 2009, p. 403.
[25] F. Gouldin, R.K. Cheng, International Workshop on Premixed Turbulent Flames. <http://eetd.lbl.gov/aet/combustion/workshop/workshop.html>.
[26] H. Kobayashi, K. Seyama, H. Hagiwara, Y. Ogami, Proc. Combust. Inst. 30 (1) (2005) 827–834.
[27] H. Kobayashi, Exp. Therm. Fluid Sci. 26 (2–4) (2002) 375–387.
[28] B.D. Videto, D.A. Santavicca, Combust. Sci. Technol. 76 (1–3) (1991) 159–164.
[29] B. Bédat, R.K. Cheng, Combust. Flame 100 (3) (1995) 485–494.
[30] C. Kortschik, T. Plessing, N. Peters, Combust. Flame 136 (1–2) (2004) 43–50.
[31] S.C. Crow, F.H. Champagne, J. Fluid Mech. 48 (1971) 547–591.
[32] W.T. Mayo Jr., in: A Discussion of Limitations and Extensions of Power Spectrum Estimation with Burst-Counter LDV Systems, International Workshop on Laser Velocimetry, West Lafayette, Indiana, Purdue University, 1974; West Lafayette, Indiana, Purdue University, 1974, pp 90–101.
[33] M.J. Tummers, D.M. Passchier, Meas. Sci. Technol. 7 (1996) 1541–1546.
[34] G.J. Smallwood, Ö.L. Gülder, D.R. Snelling, B.M. Deschamps, I. Gökalp, Combust. Flame 101 (4) (1995) 461–470.
[35] P. Griebel, P. Siewert, P. Jansohn, Proc. Combust. Inst. 31 (2) (2007) 3083–3090.
[36] J.M. Seitzman, A. Üngüt, P.H. Paul, R.K. Hanson, Proc. Combust. Inst. 23 (1) (1991) 637–644.
[37] R.K. Hanson, Proc. Combust. Inst. 21 (1) (1988) 1677–1680.
[38] C. Dasch, Appl. Opt. 31 (8) (1992) 1146–1152.
[39] A. Lutz, R. Kee, J. Miller, Sandia National Laboratories Report SAND87-8248, 1987.
[40] S.G. Davis, A.V. Joshi, H. Wang, F. Egolfopoulos, Proc. Combust. Inst. 30 (1) (2005) 1283–1292.
[41] G.P. Smith, D.M. Golden, M. Frenklach, N.W. Moriarty, B. Eiteneer, M. Goldenberg, C.T. Bowman, R.K. Hanson, S. Song, W.C. Gardiner Jr., V.V. Lissianski, Z. Qin, GRI-Mech 3.0. <http://www.me.berkeley.edu/gri_mech/>.
[42] R. Borghi, Recent Advances in the Aerospace Sciences (A 85-47304 23-31), Plenum Press, New York, 1985. pp. 117–138.
[43] C.K. Wu, C.K. Law, Proc. Combust. Inst. 20 (1) (1985) 1941–1949.
[44] R. Kee, J. Miller, G. Evans, G. Dixon-Lewis, in: A Computational Model of the Structure and Extinction of Strained, Opposed Flow, Premixed Methane–air Flames, Elsevier, 1989, pp. 1479–1494.
[45] T. Poinsot, D. Veynante, Theoretical and Numerical Combustion, R.T. Edwards, Inc., 2005.
[46] K.N.C. Bray, R.S. Cant, Proc. Math. Phys. Sci. (1991) 217–240.
[47] G. Damköhler, Z. Electrochem. 46 (1940) 601–626.
[48] S.H. El Tahry, C. Rutland, J. Ferziger, Combust. Flame 83 (1–2) (1991) 155–173.
[49] F.T.C. Yuen, Ö.L. Gülder, Proc. Combust. Inst. 32 (2) (2009) 1747–1754.
[50] P.J. Goix, I.G. Shepherd, Combust. Sci. Technol. 91 (4) (1993) 191–206.
[51] C. Rutland, A. Trouvé, Combust. Flame 94 (1) (1993) 41–57.
[52] D. Haworth, T. Poinsot, J. Fluid Mech. 244 (1992) 405–436.
[53] M. Baum, T. Poinsot, D. Haworth, N. Darabiha, J. Fluid Mech. 281 (1994) 1–32.
[54] F.N. Egolfopoulos, Proc. Combust. Inst. 25 (1) (1994) 1375–1381.
[55] D. Bradley, Proc. Combust. Inst. 24 (1) (1992) 247–262.
[56] M.S. Anand, S.B. Pope, Combust. Flame 67 (2) (1987) 127–142.
[57] K.I. Schelkin, Zh. Tekh. Fiz. 13 (1943) 520–530.
[58] D. Bradley, Symp. (Int.) Combust. 24 (1) (1992) 247–262.
[59] V. Yakhot, Combust. Sci. Technol. 60 (1) (1988) 191–214.